



Effect of tab design on large-format Li-ion cell performance



Wei Zhao^a, Gang Luo^b, Chao-Yang Wang^{a,b,*}

^aElectrochemical Engine Center (ECEC), Department of Mechanical and Nuclear Engineering, The Pennsylvania State University, University Park, PA 16802, USA

^bEC Power, State College, PA 16803, USA

HIGHLIGHTS

- A large-format Li-ion cell is studied using a 3D electrochemical model.
- Ohmic loss and non-uniform active material utilization cause performance penalty.
- Use of multiple tabs effectively improves large cell's usable energy density.
- Link of cell's energy density and current density non-uniformity is established.

ARTICLE INFO

Article history:

Received 4 November 2013

Received in revised form

11 December 2013

Accepted 11 December 2013

Available online xxx

Keywords:

Li-ion cell

Energy density

Tabs

3D

Model

ABSTRACT

Large-format Li-ion batteries are essential for vehicle and grid energy storage. Today, scale-up of Li-ion cells has not maximized the potential of available battery materials, leading to much lower energy density than their coin cell benchmarks. In this work, a 3D computational methodology based on physical and electrochemical principles underlying Li-ion cells is developed for the design of large cells. We show a significant increase in the cell's usable energy density by minimizing voltage losses and maximizing the utilization of active materials in a large cell. Specifically, a class of designs using multiple current-collecting tabs are presented to minimize in-plane electron transport losses through long electrodes, thereby achieving nearly the same energy density in large-capacity cells as would be expected from battery materials used. We also develop a quantitative relation between the current density non-uniformity in a large-format cell and the cell's usable energy density, for the first time, in the literature.

© 2014 Elsevier B.V. All rights reserved.

1. Introduction

Small Li-ion batteries have been widely used for consumer electronics due to their high power and energy density. Large Li-based batteries are believed to be essential for vehicle- and grid-energy storage enabling a sustainable energy future. How to unlock the potential of existing Li battery materials and scale up Li-ion cells to 10–100 Ah sizes without substantially lowering the cell's energy density remains a key technological challenge.

The two typical designs for large-format Li-ion batteries are the spirally wound design and stacked layer design, both involve very long electrodes. If only one pair of negative and positive current-collecting tabs is used, as illustrated in Fig. 1(a), electrons generated in the anode electrode must travel a long distance before being

collected by the negative tab. Similarly, the electrons coming from the positive tab need to be spread out over a long distance to reach all areas of the cathode electrode. Consequently, severe voltage loss is caused due to the Ohmic resistance of in-plane electron transport through thin current-collecting foils. This Ohmic loss can be very significant when the electrodes are sufficiently long as naturally occurs in large-format Li-ion cells. This situation would be exacerbated when the cell is operated at high power, which is ubiquitous in hybrid and pure electric vehicle (HEV/EV) applications.

In addition to the Ohmic loss through long current collector foils, another phenomenon contributing to low performance in large cells is uneven current density distribution and hence non-uniform utilization of active material as experimentally demonstrated recently [1]. Due to Ohmic resistances of the current collectors, an in-plane potential distribution forms along each of the electrode current collectors, reducing the local potential difference driving reaction current. Consequently, local current generation in regions distant from the two tabs is lower than that closer to the tabs that suffer less Ohmic loss in solid electrical potential. Such a

* Corresponding author. Electrochemical Engine Center (ECEC), Department of Mechanical and Nuclear Engineering, The Pennsylvania State University, University Park, PA 16802, USA. Tel.: +1 814 863 4762; fax: +1 814 863 4848.

E-mail address: cwx31@psu.edu (C.-Y. Wang).

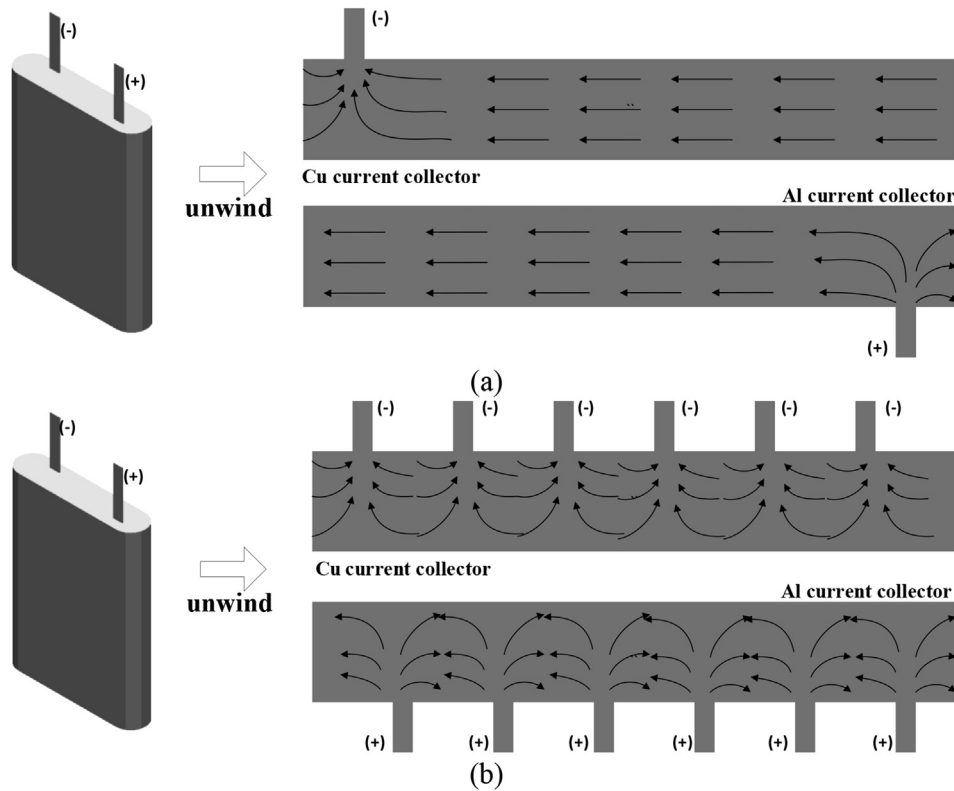


Fig. 1. Electrons transport path in the current collectors of a spirally wound cell. (a) Cell with a single pair of tabs; (b) cell with multiple pairs of tabs.

non-uniform current distribution results in non-uniform utilization rate of active materials, making average utilization of active materials in a large cell far lower than that in a small coin cell. The non-uniform utilization of active materials causes not only lower energy density than what could be expected from battery materials but also localized overcharge and overdischarge situations. Therefore, both the power and energy are compromised in large-format cells.

One solution to the above-described issue in cell upscaling is to use a plurality of tabs on the current collectors, as illustrated in Fig. 1(b). This way, the large electrode area is divided into relatively small regions, each with its own tabs for current collection. The electron transport length is shortened and the current density distribution is more uniform, leading to more uniform active material utilization. As the tab number increases, it is expected that the cell performance will approach the coin cell benchmark. However, the outcome of using excessive tabs is increased manufacture cost and decreased reliability due to tabs welded together. An optimal number of tabs thus exist for large-format cell design. A design tool for large cell structures that enables full utilization of active materials and maximum potential of energy density is highly desired.

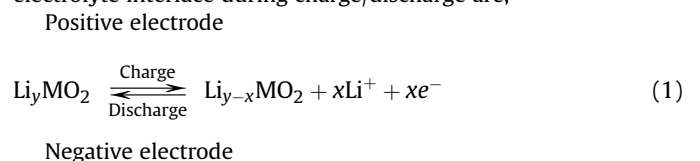
To date most of the battery models in the literature belong to 1D models [2–8]. They are inadequate to address the problem of spatially non-uniform potential and current distribution in large-format Li-ion cells. In this work, we apply a fully 3D model specially designed to study the behavior of large-format battery cells. The model has the ability to deal with coupling processes, such as species transport and electrochemical reactions during the dynamic operation of Li-ion cells. It can also take into account the 3D geometrical details of the cell, such as the cell shape, tab size, location and number, and the cell winding structures, which are uniquely important for large-format cells.

The purpose of the present work is three-fold. Firstly, we quantify the significant performance loss in large-format cells relative to the coin cell benchmark. The fundamental reasons for such a performance penalty will be elucidated. Secondly, we demonstrate a way to recover the performance loss by optimizing designs of large Li-ion cells using multiple tabs on current collectors, and the effect of tab number on cell performance is assessed. Thirdly, we develop a quantitative relationship between the current density non-uniformity and the cell's usable energy density. The ultimate goal is to help find directions in boosting battery performance closest to its theoretical material capacity under practical operating conditions.

2. 3D Li-ion cell model

2.1. Model description

The large-format Li-ion cell of interest has a spirally wound structure, as schematically shown in Fig. 2. The long electrode sheet consists of the negative electrode current collector (Cu), negative electrode (Li_xC_6), separator, positive electrode (Li_yMO_2), and the positive current collector (Al). During operation, current is applied to the cell through positive tab and negative tab, located on the positive current collector and negative current collector, respectively. The electrochemical reactions occurring at the electrode/electrolyte interface during charge/discharge are,



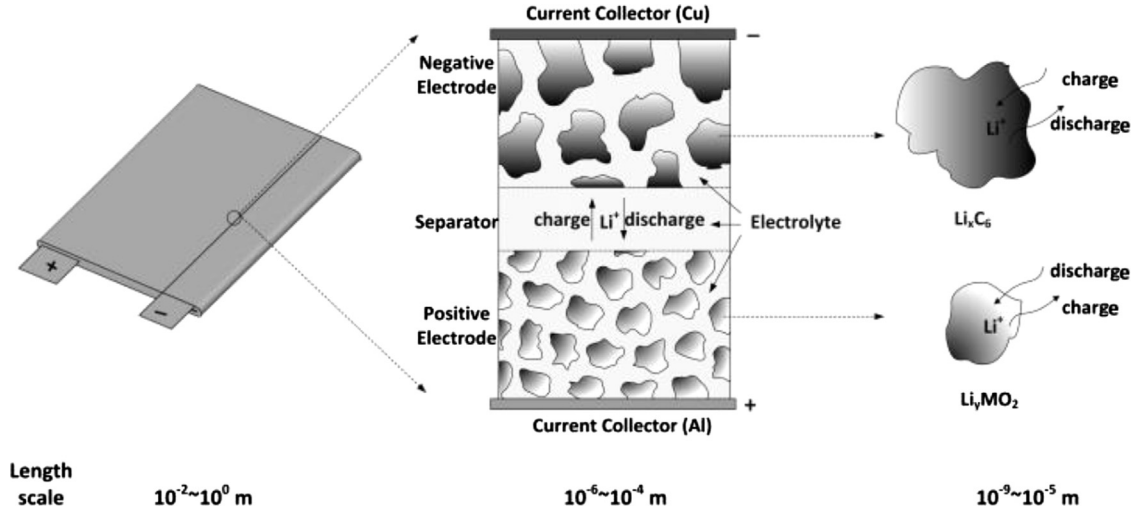
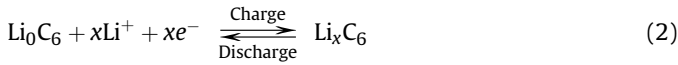


Fig. 2. Schematic of the large spirally wound cell and the multiscale physical and electrochemical processes within cell during charge/discharge.



A volume-averaged electrochemical and transport model has been developed to study such large-format Li-ion cells [9]. Its 1D version has been extensively validated by experimental data over a wide range of temperatures and C-rates [10], and its three-dimensional version was recently validated against local current density distributions measured by Zhang et al. [1], for the first time in the literature [11]. Other key features of the model include multidimensionality, multiscale, an accurate material property database and efficient numerical algorithms offered through Autolion, a commercial software package for analyses of Li-ion batteries and systems. These model features are essential for dealing with the various physical processes within cells, as shown in Fig. 2, and therefore can be used for predicting the above-mentioned behaviors that are uniquely present in large-format Li-ion cells. The model is briefly summarized in the following with details to be found in Ref. [9].

2.2. Governing equations

Charge conservation (solid phase)

$$\nabla \cdot (\sigma^{\text{eff}} \nabla \phi_s) = j^{\text{Li}} \quad (3)$$

Charge conservation (electrolyte phase)

$$\nabla \cdot (\kappa^{\text{eff}} \nabla \phi_e) + \nabla \cdot (\kappa_D^{\text{eff}} \nabla \ln c_e) = -j^{\text{Li}} \quad (4)$$

Species conservation (electrolyte phase)

$$\frac{\partial(\epsilon_e c_e)}{\partial t} = \nabla \cdot (D_e^{\text{eff}} \nabla c_e) + \frac{1-t_+^0}{F} j^{\text{Li}} \quad (5)$$

Species conservation (solid phase)

$$\frac{\partial c_s}{\partial t} = \frac{D_s}{r^2} \frac{\partial}{\partial r} \left(r^2 \frac{\partial c_s}{\partial r} \right) \quad (6)$$

Eqs. (3)–(5) are solved on the macroscopic 3D space of the battery cell, where detailed potential and Li concentration distribution can be obtained from the model solution. Eq. (6) is used to describe the solid-state diffusion process which occurs within the

active material particles with the size on the order of nm– μm [12]. This equation is solved separately in a microscopic space. In this work, all the active material particles are considered to be spherical.

The governing equations are coupled through volumetric current density j^{Li} , which quantifies the rate of lithium intercalation and de-intercalation reactions at the interface of active material particles and electrolyte. Butler–Volmer equation is generally assumed to describe the reaction kinetics

$$j^{\text{Li}} = a_s i_0 \left\{ \exp \left[\frac{\alpha_a F}{RT} \eta \right] - \exp \left[-\frac{\alpha_c F}{RT} \eta \right] \right\} \quad (7)$$

The local surface over-potential, η , which controls the kinetic reaction rate, is defined as the difference between the electronic and electrolyte phase potential, with respect to the open circuit potential (OCP),

$$\eta = \phi_s - \phi_e - U \quad (8)$$

The exchange current density, i_0 , is a function of Li concentration in both electrolyte and solid active materials.

$$i_0 = k(c_e)^{\alpha_a} (c_{s,\text{max}} - c_{s,e})^{\alpha_a} (c_{s,e})^{\alpha_c} \quad (9)$$

where $c_{s,\text{max}}$ is the maximum Li concentration that can be taken by the active materials, and $c_{s,e}$ is the Li concentration at the electrode/electrolyte interface. The OCP value is a function of local surface stoichiometry, defined as $x = c_{s,e}/c_{s,\text{max}}$ [13,14].

To account for the tortuosity effect in the porous electrodes and separator, Bruggeman correction is used such that $D_e^{\text{eff}} = D_e \epsilon_e^{1.5}$, $\kappa^{\text{eff}} = \kappa_e \epsilon_e^{1.5}$ and $\sigma^{\text{eff}} = \sigma_e \epsilon_s^{1.5}$. ϵ_e and ϵ_s are the volume fraction of electrolyte phase and solid phase, respectively. The diffusional conductivity κ_D^{eff} in Eq. (4) is defined by concentration solution theory [2] as

$$\kappa_D^{\text{eff}} = \frac{2RT\kappa^{\text{eff}}}{F} (t_+^0 - 1) \left(1 + \frac{d \ln f_{\pm}}{d \ln c_e} \right) \quad (10)$$

where $(t_+^0 - 1)(1 + (d \ln f_{\pm}/d \ln c_e))$ is the thermodynamic factor and its value in electrolyte with LiPF_6 as a function of Li concentration in electrolyte, c_e , is taken from Ref. [15].

2.3. Initial and boundary conditions

The solid phase and electrolyte concentration distributions are prescribed at the beginning of simulation as initial conditions.

$$c_e = c_{e,0}, c_s = c_{s,0} \quad (11)$$

Because the electrolyte is confined in the electrodes and separator, zero flux boundary conditions are applied for Eqs. (4) and (5) at the interface between the current collector and electrode.

$$\frac{\partial c_e}{\partial n} = 0, \frac{\partial \phi_e}{\partial n} = 0 \quad (12)$$

Current boundary condition is applied directly at the top surface of the positive and negative tabs.

$$-\sigma_{\text{tab}} \frac{\partial \phi_s}{\partial n} = \frac{I_{\text{app}}}{A_{\text{tab}}} \quad (13)$$

where A_{tab} is the cross sectional area of the tabs. At all other boundaries,

$$\frac{\partial \phi_s}{\partial n} = 0 \quad (14)$$

2.4. Numerical procedures

The governing equations are discretized using finite volume method (FVM) and solved along with their initial and boundary conditions, using the user-coding capability of the commercial computational fluid dynamics (CFD) package, STAR-CD. All the equations are solved sequentially at each time step and the calculation proceeds to the next time step if the convergence criteria are met. For constant rate charge/discharge condition, the charge balance over the entire cell is used as a critical convergence criterion.

$$\epsilon_I = \min \left(\left| \frac{I_a - I_{\text{app}}}{I_{\text{app}}} \right|, \left| \frac{I_c - I_{\text{app}}}{I_{\text{app}}} \right| \right) \quad (15)$$

where I_a and I_c are the total output current of anode and cathode electrode, respectively.

$$I_a = \int_{V, \text{anode}} j^{\text{Li}} dV \quad (16)$$

$$I_c = \int_{V, \text{cathode}} j^{\text{Li}} dV \quad (17)$$

ϵ_I is chosen to be sufficiently small ($<0.01\%$) to ensure physically meaningful results.

3. Results and discussion

A 40 Ah large-format Li-ion cell is chosen for the present study. The cell has a graphite anode and an NMC cathode. Table 1 lists the cell design parameters. The cell has a total electrode length of 512 cm and electrode width of 20.5 cm. Both the Cu and Al current collecting foils are double-side coated with active materials. The separator is placed between the two electrode sheets and the multilayer structure is wound to form a prismatic cell. A computational mesh resolving the detailed cell winding structure and tab configuration is shown in Fig. 3. The present model for NMC–Graphite system has been extensively validated by experimental

Table 1
Design parameters of the 40 Ah Li-ion cell.

| | Positive electrode | Negative electrode |
|---------------------------|--|-------------------------|
| Chemistry | $\text{Li}_y\text{Co}_{1/3}\text{Ni}_{1/3}\text{Mn}_{1/3}\text{O}_2$ | Li_xC_6 |
| Loading amount | 27 mg cm^{-2} | 12 mg cm^{-2} |
| Electrode thickness | 120 μm | 110 μm |
| Foil thickness | 20 μm | 10 μm |
| Separator thickness | 40 μm | |
| Electrolyte | EC/EMC/DMC 1 M LiPF_6 | |
| NP ratio | 1.13 | |
| Electrode width (W) | 20.5 cm | |
| Electrode length (L) | 512 cm | |
| Total active area (A) | 20,992 cm^2 | |
| Nominal capacity (C) | 40 Ah | |

discharge curves over a wide range of temperatures and C-rates in Ref. [10].

The baseline case has one pair of tabs welded outward from the end edges of the long sides of current collectors. Two types of tab arrangement are considered here, as illustrated in Fig. 4. Depending on the relative positions of the positive and negative tabs, they are named as co-located (CO) tab design and counter-located (CU) tab design. The CO design has both positive and negative tabs located at the leading edge ($z = 0$) of the current collectors. In the CU design, the negative tab is located at the trailing edge ($z = L$) of the Cu current collector and the positive tab is located at the leading edge ($z = 0$) of the Al current collector. Several important physiochemical parameters used in the model are listed in Table 2.

Fig. 5 shows the calculated 1 C discharge curves for the two cell designs. The corresponding discharge curve of a coin cell with the exact same electrode formulation and cell assembly in small surface area is depicted for comparison. It is evident that the performance of large-format cells, both CO and CU designs, is far inferior to the coin cell performance. Table 3 lists the energy density calculated from the modeling data for different cells at several C-rates. The data is normalized by the energy density of coin cells at 1 C discharge for better comparison. At 1 C discharge, the CO cell and CU cell can achieve only 39% and 52% of the energy density of coin cells, respectively. At higher C-rate operation, the performance loss is even more severe. For example, the CU cell cannot go to 2 C or 3 C discharge because the cell voltage will drop below 2.5 V at the beginning of discharge. This is the evidence that in scaling up Li-ion cells from coin cells or small cells to large-format cells, performance loss could be significant. Therefore, engineering optimization for the cell design must be carried out in addition to the material development in order to attain superior performance at large-format.

Besides the common fact that CO and CU cells both have significant performance penalty compared with the coin cell, their discharge curves behave very differently. At the beginning of discharge, the voltage loss relative to the coin cell is 0.163 V in the CO cell and 0.824 V in the CU cell, respectively. The CO cell thus has a higher power output than the cell with CU design. However, the discharge curve of the CO cell exhibits a much steeper slope, indicating a rapidly increased voltage loss during discharge. Thus, although having a better initial performance, the CO cell drops below 2.5 V cut-off voltage at an earlier discharge stage (at DoD = 41.8% or SOC = 58.2%), while the CU cell can reach the point where DoD = 64.8% or SOC = 35.2%.

The source of performance loss in large-format cells and the difference in the behaviors of CO and CU cells can be explained by examining internal variables distributions predicted by the model. Since the large cell has a high aspect ratio ($L \gg W$), we are only interested in the variable distribution along the electrode length direction, i.e. z -direction defined in Fig. 3. At each location along the

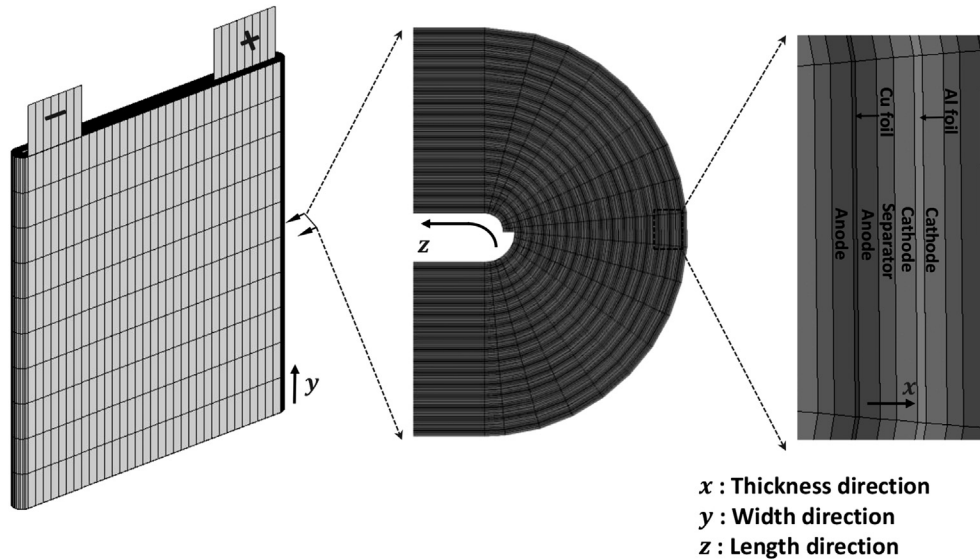


Fig. 3. Computational mesh of the large-format spirally wound cell.

z -direction, the variables of interest are averaged across the electrode width direction (y -direction). Here, solid potential, current density, and local SOC along the current collectors are the variables of interest, and their distributions are displayed in Figs. 6–8, respectively. Three time instants, corresponding to the beginning, middle and end of discharge, are chosen for analysis.

Fig. 6(a) shows the solid potential profile along Al and Cu current collectors of the CO cell. At the beginning of discharge ($t = 1$ s), the solid potential gradient in both current collectors is mainly confined in the region very near the two tabs. The local potential difference that drives the electrochemical reactions decreases along the electrode length direction. Therefore, a highly non-uniform current density distribution along the electrode length direction is formed, as shown in Fig. 7(a). Note that the local current density is normalized by the average current density, defined as the total discharge current divided by the electrode area. At $t = 1$ s, in the area near the tabs the current density is as high as ~ 10 times of the average current density, while the current density is almost zero at the electrode area near the trailing edge of the cell. This is the indication that the total current is mostly contributed from the reaction of electrode materials that are located close to the tabs. It can be estimated that the first 1/3 of the electrode contributes 98% of the total current at $t = 1$ s. The high current density concentrating near the tabs region results in a relatively small Ohmic loss in the current collectors, explaining the higher initial voltage of CO cell in Fig. 5.

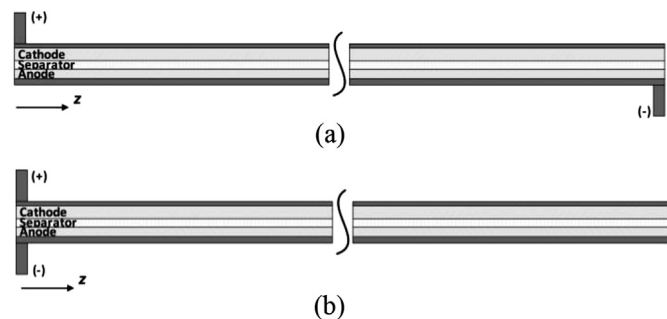


Fig. 4. Schematic of the unwound Li-ion cell with one pair of tabs: (a) counter-located tab design (CU-design); (b) co-located tab design (CO-design). (The drawing is not to scale.)

The voltage loss along current collectors ($\Delta\phi_s = \phi_{s,z=L} - \phi_{s,z=0}$) is 0.07 V in the Al foil and 0.08 V in the Cu foil, respectively.

The highly non-uniform current density distribution of CO cell at the beginning of discharge is the root cause for the subsequent rapid voltage drop shown in Fig. 5. The non-uniform initial current density distribution results in significant non-uniform utilization of active material. One can quantify the degree of active material utilization by local SOC ($iSOC$), which is defined by coulomb counting as,

$$iSOC(z, t) = 1 - \frac{\int_0^t i_a(z, \tau) d\tau}{\frac{C}{A}} \quad (18)$$

where i_a is the local current density. Fig. 8(a) plots the $iSOC$ distribution for the CO cell. Due to the very high current density near the tabs region, the active material in that region is consumed faster and becomes depleted more quickly than the region far from the tabs. The $iSOC$ is initially uniform everywhere and equal to the fully charged state. At $t = 750$ s, $iSOC(z = 0) = 28\%$ and $iSOC(z = L) = 96\%$. At the end of discharge, where $t = 1500$ s, $iSOC(z = 0) = 5\%$ and $iSOC(z = L) = 89\%$, respectively. This means the majority of the active material near the trailing edge of the electrode has not been used when the discharge process is terminated. This non-uniform utilization of active material brings down the cell voltage by two mechanisms. Firstly, as the active material near the tabs area becomes depleted, the current has to be supplied by the active material downstream. As shown in Fig. 7(a), the current density peak propagates toward the downstream of electrodes as the discharge goes on. This increases the electrons transport length and therefore the Ohmic loss through the current collectors. Secondly, the local OCP decreases with the consumption of active material. In Fig. 6(a), it can be observed that as the discharge proceeds, the solid potential gradient penetrates towards the downstream of electrodes and the voltage loss in the current collectors becomes larger. At $t = 750$ s, $\Delta\phi_s = 0.37$ V and 0.44 V in Al and Cu current collectors, respectively. At the end of discharge, where $t = 1500$ s, $\Delta\phi_s = 0.64$ V and 0.54 V, in Al and Cu current collectors, respectively. Consequently, although the CO cell has a higher initial discharge voltage, this higher voltage cannot be sustained and it drops more quickly than the CU cell and hits the cut-off voltage earlier.

Table 2
Physiochemical parameters used in the model.

| Parameter | Unit | Cu foil | Negative electrode | Separator | Positive electrode | Al foil |
|-------------------------------------|---------------------------------|-------------------------|---------------------------------|------------------------|--------------------------------|-------------------------|
| Density | kg cm ⁻³ | 8960 × 10 ⁻⁶ | 1200 × 10 ⁻⁶ | 525 × 10 ⁻⁶ | 2860 × 10 ⁻⁶ | 2700 × 10 ⁻⁶ |
| Electron conductivity | S cm ⁻¹ | 5.8 × 10 ⁵ | 1.0 [7–9] | | 0.1 [7,8] | 3.538 × 10 ⁵ |
| Maximum Li capacity | mol cm ⁻³ | | 0.031 | | 0.0518 | |
| Stoichiometry at 0%/100% SOC | | | 0.042/1.0 | | 0.98/0.39 | |
| Charge transfer coefficient | | | 0.5 | | 0.5 | |
| Reference exchange current density | A m ⁻² | | 26 [7,8] | | 2.0 [10] | |
| Diffusion coefficient – solid phase | cm ² s ⁻¹ | | 9.0 × 10 ⁻¹⁰ [16,17] | | 1.5 × 10 ⁻¹⁰ [8,10] | |
| Bruggeman tortuosity exponent | | | 1.5 | 1.5 | 1.5 | |
| Transference number | | | | 0.363 [9] | | |
| Porosity | | | 0.46 | 0.4 | 0.29 | |
| Particle radius | μm | | 10 | | 3 | |
| Initial electrolyte concentration | M | | | 1 | | |
| Cell temperature | °C | | | 25 | | |

The CU cell has a unique tab configuration in which the positive tab is located at the leading edge ($z = 0$), and the negative tab is at the trailing edge ($z = L$). Thus, the electrons transport length for any local section of the cell remains constant and equal to the total electrode length L . Consequently, different solid potential distribution evolves in contrast to the CO cell, as shown in Fig. 6(b). The local potential difference is more evenly distributed along the electrode length, compared with that of CO cell, leading to more uniform current density distribution, as illustrated in Fig. 7(b). In addition, the current density of the CU cell exhibits almost symmetric distribution. At the beginning of discharge ($t = 1$ s), the current density is higher at the two ends of the electrode and smaller in the cell center. The current density peak propagates from both ends towards the center as the discharge proceeds. Due to the symmetric and more uniform current density distribution, the local SOC also is lowered more symmetrically and uniformly than that of CO cell, as shown in Fig. 8(b). The total discharge time of CU cell is therefore longer than the CO cell because of more uniform utilization of active materials. However, at the beginning of discharge, due to the longer electrons transport length and hence higher Ohmic loss than the CO cell, the CU cell has a lower output voltage than that of CO cell.

The above analysis demonstrates that large-format Li-ion cells, fabricated in spirally wound structures and equipped with only a single pair of tabs, exhibit significant power and energy loss. It is imperative to explore ways to improving cell design in order to regain the performance corresponding to a coin cell made of the same materials.

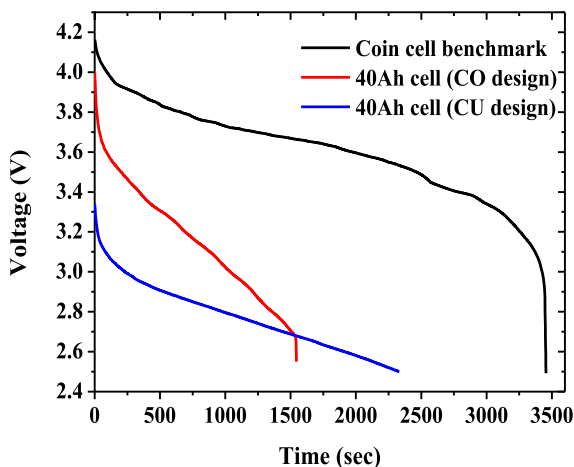


Fig. 5. Simulated 1 C discharge curves of baseline cases and the comparison with coin cell benchmark.

One solution is to use a plurality of tabs placed strategically on the current collectors in the electrode length direction. This will reduce the Ohmic loss along the current collectors and promote the uniformity of reaction current distribution, thereby improving the cell performance. The number of tabs, however, should be kept minimal so as to reduce manufacture cost and increase reliability. In practice, however, it is largely based on battery designers' empirical experience to determine how many tabs would be necessary to mitigate the performance loss. Trial and error has been widely adopted for battery design, which becomes more expensive and time consuming when used for the design of large-format cells. The 3D battery model described in the present work is then a powerful tool for this purpose.

Fig. 9 sketches various multi-tab configurations for CO cell and CU cell. In the current study, the tabs are evenly spaced on the current collectors along the electrode length direction. The resulting effect is dividing a long electrode into small sections that are connected in parallel by tabs. Specifically, for the CU design, the total electrode is divided into $(N-1)$ sections, where N is the total tab number. The total electrode of the CO design is divided into $(N-2)$ sections. Fig. 10 shows the effect of tab number on the 1 C discharge performance of CO and CU cell. It is evident that adding multiple tabs effectively boosts the performance for both CO and CU cell. The cell energy densities of the different designs are compared and listed in Table 3. It is noteworthy that by adding only one positive tab in the CU cell and two tabs in the CO cell, the performance for both cell designs can be greatly improved from the baseline cases. For example, at 1 C discharge, the energy density is increased from 52% to 89% for the CU cell and from 39% to 80% for the CO cell, respectively. The same trend holds true for higher C-rate discharge. Further increasing the tab number would make the cell performance approach the coin cell benchmark.

Table 3
Comparison of calculated energy density of various cell designs.

| | 1 C discharge | 2 C discharge | 3 C discharge |
|----------------|---------------|---------------|---------------|
| Coin cell | 100% | 87% | 75% |
| Baseline cell | | | |
| 2 tabs (CO) | 39% | 10% | 3.3% |
| 2 tabs (CU) | 52% | N/A | N/A |
| Multi-tab cell | | | |
| 3 tabs (CU) | 89% | 68% | 62% |
| 4 tabs (CO) | 80% | 62% | 44% |
| 5 tabs (CU) | 96% | 84% | 71% |
| 6 tabs (CO) | 97% | 84% | 71% |
| 7 tabs (CU) | 98% | 85% | 73% |
| 8 tabs (CO) | 99% | 85% | 73% |

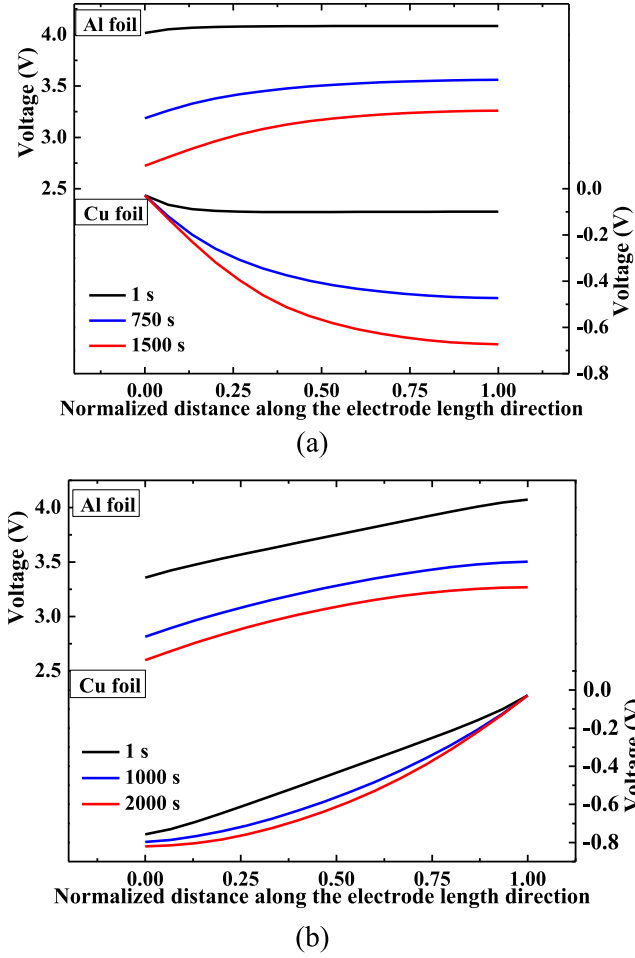


Fig. 6. Solid potential distribution on current collectors along the electrode length direction: (a) CO design cell; (b) CU design cell.

It is argued earlier and generally believed that maintaining uniform current density distribution is critical for boosting the performance of large-format Li-ion cells. Therefore it is of great interest to develop a quantitative relationship between the uniformity of current density distribution and cell's overall energy density.

A quantitative measure of current density uniformity must take account of the spatial variation of current density along the electrode length. It should also consider the change of the variation with respect to time, given the fact that discharge/charge of battery is an intrinsically transient process. In statistics and probability theory, standard deviation is used to show how much variation exists from the mean value. Here we define a time-averaged standard deviation as an index to evaluate the current density distribution uniformity during a discharge/charge process, i.e.

$$\bar{\sigma} = \sqrt{\frac{\int_{t_0}^t \sigma(\tau)^2 d\tau}{\int_{t_0}^t d\tau}} \quad (19)$$

where $\sigma(\tau)$ is the instantaneous standard deviation of the local current density distribution, which can be calculated by

$$\sigma(\tau) = \sqrt{\frac{1}{N} \sum_{i=1}^N (i_i(\tau) - i_{\text{avg}})^2} \quad (20)$$

where the subscript i represents each control volume discretized in the computational mesh and N denotes the number of total control volumes. In practice, the battery model uses finite time steps. Eq. (20) then becomes,

$$\bar{\sigma} = \sqrt{\frac{\sum_{i=1}^{N_t} \sigma_i^2 \cdot \Delta t_i}{\sum_{i=1}^{N_t} \Delta t_i}} \quad (21)$$

where Δt_i is the i th time step and N_t is the total number of time steps. Noting that $\bar{\sigma}$ has the same unit as that of current density, one can normalize $\bar{\sigma}$ by the average current density for better comparison, which is termed as the current density non-uniformity factor in later discussions.

Fig. 11(a) shows such a direct link of the cell's energy density with the current density non-uniformity factor for CO cells and CU cells with different tab numbers. It is clearly demonstrated that the current density uniformity strongly affects the cell's energy density. For both designs, as the tab number increases, the current density distribution becomes more uniform (indicated by the decrease of $\bar{\sigma}$) and the cell performance, i.e. the energy density, improves substantially.

Another observation from Fig. 11(a) is that while the both curves for the CO cell and CU cell indicate strong correlation between the cell's energy density and current density non-uniformity factor,

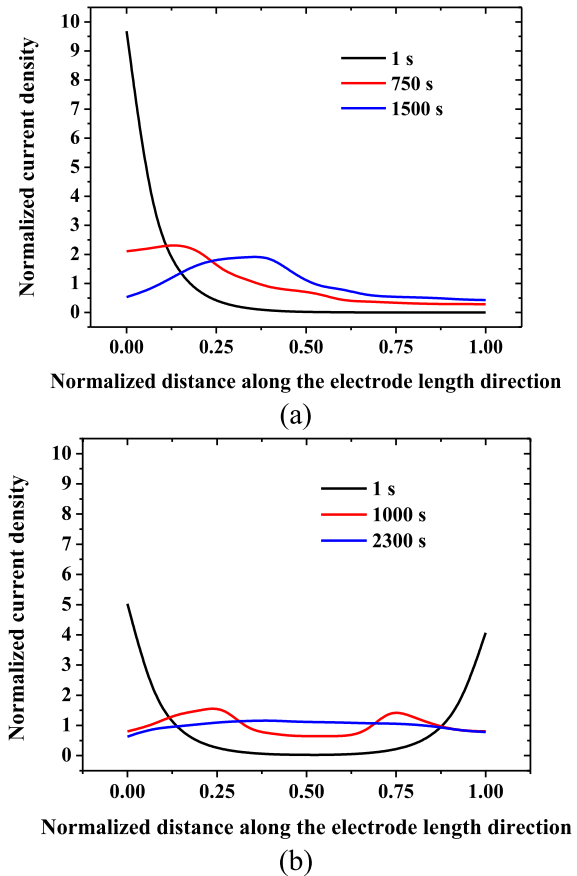


Fig. 7. Current density distribution on current collectors along the electrode length direction: (a) CO design cell; (b) CU design cell.

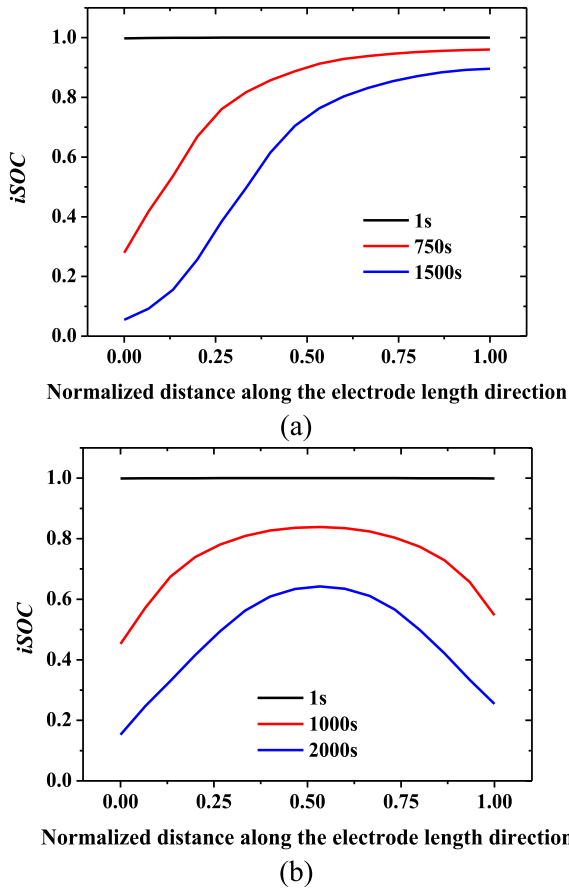


Fig. 8. Local SOC distribution along the electrode length direction: (a) CO design cell; (b) CU design cell.

they quantitatively differ. Therefore caution must be taken when comparing cells with vastly different structure designs. Finally it is worth noting that for cells with current density non-uniformity factor between 0.1 and 0.2, the cell's energy density could be lowered by 10% from its maximum realizable by a coin cell.

The significance of these quantitative results, shown in Fig. 11(a) for the first time in the literature, is that they point out new ways to increase the cell's energy density besides material innovations. The potential through cell architecture innovation is great, amounting to 50%-level improvement. In addition, Fig. 11(a) quantifies the importance of achieving uniform current distribution in large-format Li-ion cells, an engineering topic that has been largely overlooked. Only recently Zhang et al. [1] began the measurements

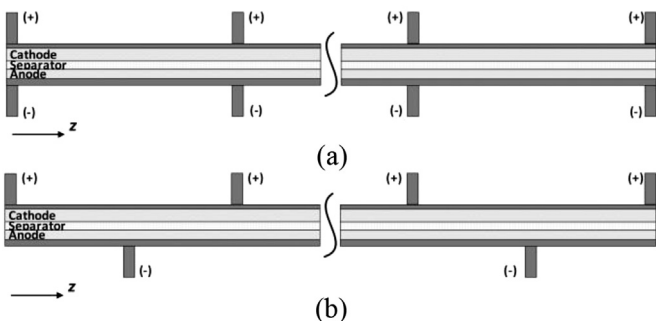


Fig. 9. Multiple-tab configuration for the large-format Li-ion cell: (a) CO-design; (b) CU-design. (The drawing is not to scale.)

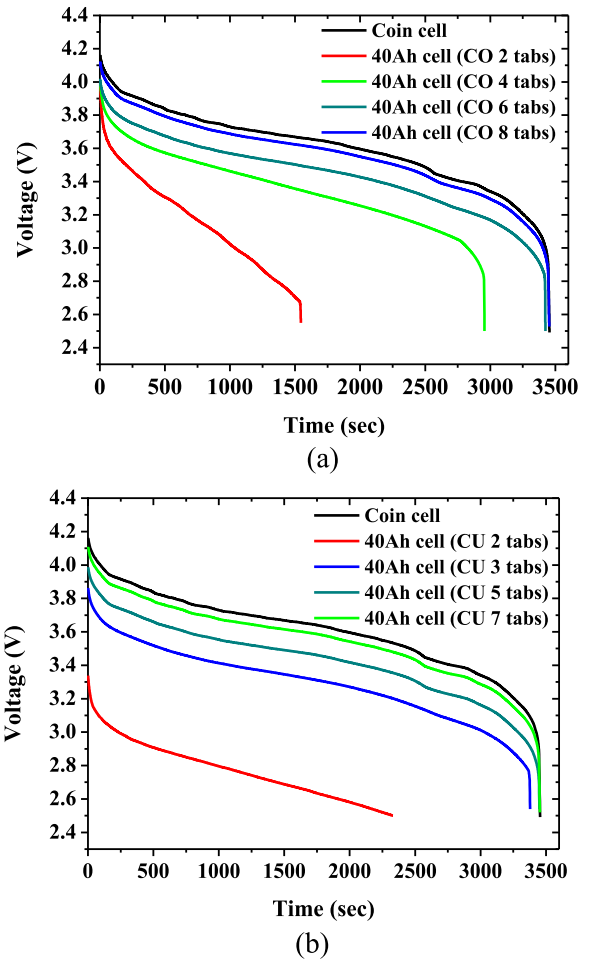


Fig. 10. Comparison of discharge performance among different cell designs: (a) CO design cell; (b) CU design cell.

of local current density distribution as part of large-format battery diagnostics.

Inspired by the results shown in Fig. 11(a), we have undertaken a corresponding experimental effort to verify the quantitative relationship between the cell's energy density and current density non-uniformity as discovered in Fig. 11(a). We used a 2.4 Ah lithium iron phosphate (LFP)/graphite cell fixture that is available in our laboratory and re-configured with a varying number of tabs. Details of this companion experimental work are described in Ref. [18]. The present model results are now superimposed with the experimental data of 2.4 Ah LFP/graphite cells in Fig. 11(b). Despite differences in size (the 2.4 Ah cell is limited by our fabrication capability in the lab) and cathode material (LFP cathode has been extensively developed in our lab), the trend and magnitude of cell energy density vs. current density non-uniformity are clearly consistent between the model predictions and experiments. More quantitative comparisons using the NMC chemistry and the exact cell size need to be carried out in the future.

Other interesting questions await further research and clarification. Do the two curves depicted in Fig. 11(a) for the two extreme cell structures represent the upper and lower bounds of all cell designs? Does a fan-shaped correlation between energy density and current density non-uniformity factor exist universally for other battery materials? What are parameters, mechanisms or structures controlling the curve slope and how one can achieve the smallest slope possible?

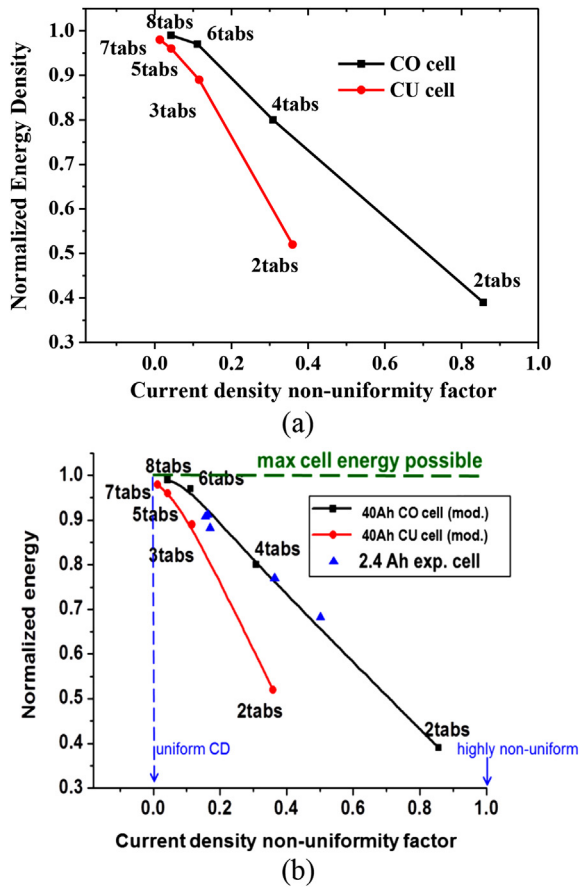


Fig. 11. Relationship between cell's energy density and the current density non-uniformity. The energy density is for 1 C discharge process and is normalized by the coin cell energy density, i.e. the maximum achievable energy density with the battery materials used. (a) Model results for 40 Ah NMC/graphite cells; (b) comparison of model results for 40 Ah cells with experimental data for 2.4 Ah cells.

4. Conclusions

Engineering optimization is imperative to boost performance of large-format Li-ion cells in order to achieve the full potential of existing battery materials. A multidimensional, electrochemical and transport coupled model has been applied, for the first time, to address current density distribution uniquely present in large-format Li-ion cells. It is shown that for a large-format cell with spirally wound structure, significant performance loss is induced compared with the coin cell having the same active materials and electrode formulation. It is found that the performance loss results from the electrons transport through long current collectors, which not only causes large Ohmic resistance, but also creates non-uniform utilization of active materials. It is further shown that the tab number and location can mitigate the Ohmic loss, thereby significantly improving the cell performance. Two tab configurations, namely counter-located (CU) design and co-located (CO) design, have been proposed and their impact on the cell performance has been quantified. We also presented a quantitative correlation between the cell's energy density and current distribution non-uniformity and provided preliminary experimental confirmation, for the first time in the literature.

Acknowledgments

Partial support of this work by DOE CAEBAT Program is greatly acknowledged. We are grateful to EC Power for offering numerical

algorithms and materials database through its AutoLion software and to Dr. Christian E. Shaffer for useful discussions.

Nomenclature

| | |
|------------------|---|
| A | total active area, cm^2 |
| A_{tab} | tab cross sectional area, cm^2 |
| a_s | specific active surface area for an electrode, $\text{cm}^2 \text{cm}^{-3}$ |
| C | nominal cell capacity, Ah |
| c | lithium concentration in phase, mol cm^{-3} |
| D | diffusion coefficient of lithium species, $\text{cm}^2 \text{s}^{-1}$ |
| F | faraday's constant, 96487 C mol^{-1} |
| f_{\pm} | mean molar activity coefficient of the electrolyte |
| I_{app} | applied discharge current, A |
| i_0 | exchange current density, A cm^{-2} |
| $i\text{SOC}$ | local state of charge |
| j | volumetric reaction current, A cm^{-3} |
| k | rate constant for an electrode reaction |
| L | length of the electrode, cm |
| R | universal gas constant, $8.3143 \text{ J mol}^{-1} \text{ K}^{-1}$ |
| r | radial coordinate across a spherical particle, cm |
| SOC | state of charge |
| T | temperature, K |
| t | time, s |
| t_+^0 | transference number of lithium ion |
| U | equilibrium potential of an electrode reaction, V |
| W | width of the electrode, cm |
| x | coordinate along the electrode thickness, cm |
| y | coordinate along the electrode width, cm |
| z | coordinate along the electrode length, cm |

Greek

| | |
|----------------|--|
| α_a | anodic transfer coefficient |
| α_c | cathodic transfer coefficient |
| ϵ | volume fraction of a phase |
| ϵ_I | error of charge of balance |
| η | surface overpotential of an electrode reaction, V |
| κ | ionic conductivity of electrolyte, S cm^{-1} |
| κ_D | diffusional conductivity, A cm^{-1} |
| σ | electronic conductivity of an electrode, S cm^{-1} |
| $\sigma(\tau)$ | instantaneous standard deviation of current density distribution, A cm^{-2} |
| $\bar{\sigma}$ | time-averaged standard deviation of current density distribution, A cm^{-2} |
| ϕ | electrical potential in a phase, V |

Subscripts

| | |
|-----|-------------------|
| 0 | initial value |
| a | anode |
| c | cathode |
| e | electrolyte phase |
| s | solid phase |

Superscripts

| | |
|-----|-----------------|
| eff | effective |
| Li | lithium species |

References

- [1] G. Zhang, C.E. Shaffer, C.Y. Wang, C.D. Rahn, J. Electrochem. Soc. 160 (2013) A610–A615.
- [2] M. Doyle, T.F. Fuller, J. Newman, J. Electrochem. Soc. 140 (1993) 1526–1533.
- [3] T.F. Fuller, M. Doyle, J. Newman, J. Electrochem. Soc. 141 (1994) 1–10.
- [4] C.Y. Wang, V. Srinivasan, J. Power Sources 110 (2002) 364–376.
- [5] J. Wu, V. Srinivasan, J. Xu, C.Y. Wang, J. Electrochem. Soc. 149 (2002) A1342–A1348.
- [6] V. Srinivasan, C.Y. Wang, J. Electrochem. Soc. 150 (2003) A98–A106.
- [7] K. Smith, C.Y. Wang, J. Power Sources 161 (2006) 628–639.

- [8] W. Fang, O.J. Kwon, C.Y. Wang, *Int. J. Energy Res.* 34 (2010) 107–115.
- [9] G. Luo, C.Y. Wang, Chapter 6 in *Lithium-ion Batteries: Advanced Materials and Technologies*, CRC Press, 2011.
- [10] Y. Ji, Y. Zhang, C.Y. Wang, *J. Electrochem. Soc.* 160 (2013) A636–A649.
- [11] G. Luo, C.E. Shaffer, J. Kapulson, C.Y. Wang, to be published, 2013.
- [12] D. Linden, T.B. Reddy, *Handbook of Batteries*, third ed., McGraw-Hill, New York, NJ, 2001.
- [13] M.W. Verbrugge, B.J. Koch, *J. Electrochem. Soc.* 150 (2003) A374–A384.
- [14] N. Yabuuchi, Y. Makimura, T. Ohzuku, *J. Electrochem. Soc.* 154 (2007) A314–A321.
- [15] L.O. Valoen, J.N. Reimers, *J. Electrochem. Soc.* 152 (2005) A882–A891.
- [16] V. Srinivasan, J. Newman, *J. Electrochem. Soc.* 151 (2004) A1530–A1538.
- [17] D.W. Dees, S. Kawauchi, D.P. Abraham, J. Prakash, *J. Power Sources* 189 (2009) 263–268.
- [18] G. Zhang, C.E. Shaffer, C.Y. Wang, C.D. Rahn, *J. Electrochem. Soc.* 160 (2013) A2299–A2305.